Hybrid RANS/LES simulations of a cavitating flow in Venturi

Jean Decaix, Eric Goncalvès da Silva

HYBRID RANS/LES SIMULATIONS OF A CAVITATING FLOW IN VENTURI

Jean DECAIX
Department of Systems Engineering
University of Applied Science Western Switzerland
Route du Rawyl 47 / CH-1950 Sion / Switzerland
jean.decaix@hevs.ch

Eric Goncalves
LEGI
1025 Rue de la Piscine, 38 400 Saint Martin d'Hères, France
eric.goncalves@legi.grenoble-inp.fr

ABSTRACT

A numerical investigation of the behaviour of a cavitation sheet developing along a Venturi geometry has been performed using a compressible one-fluid RANS solver. The interplay between turbulence and cavitation regarding the unsteadiness and the structure of the flow is complex and not well understood. This constitutes a determinant point to accurately simulate the dynamic of sheet cavities. Various turbulent approaches are tested: a new Scale-Adaptive model (SAS) and the Detached Eddy Simulation (DES). 3D simulations are compared with the experimental data. An oblique mode of the sheet is put in evidence.

INTRODUCTION

Cavitation is a significant engineering phenomenon that occurs in fluid machinery, fuel injectors, marine propellers, nozzles, underwater bodies, etc. Such flows are characterized by important variations of the local Mach number (due to the drastic diminution of the speed of sound in the mixture), large density ratio between the liquid and the vapor phases, small-scale turbulence interactions and non equilibrium thermodynamic states.

Considerable efforts have been realized to understand the fundamental physics of cavitation phenomena concerning the dynamic of both sheet and cloud cavitation. Cavitation sheets that appear on solid bodies are characterized by a closure region which always fluctuates, with the presence of a re-entrant jet. Partial cavitation can be classified as either closed or open attached cavitation, depending on the flow in the cavity closure region (Laberteaux & Ceccio (2001)). Observations on hydrofoils with high-speed motion pictures put in evidence the three-dimensional structures associated with the phenomena (de Lange & de Bruin (1998)). To distinguish between various directions of the re-entrant flow, the term side-entrant jet was introduced. This term refers to the part of the jet that has a strong spanwise velocity component directed into the cavity originating from the sides. The term re-entrant jet is reserved for the flow originating from the part of the cavity where the closure is more or less perpendicular to the incoming flow. Both jets may form an equally important source for the sheddings (Foeth *et al.* (2006)).

Recently, an experimental analysis of a pulsating cavitation sheet made appear the presence of a bifurcation of the cavitation sheet behaviour (Prothin *et al.* (2012)). It seemed that when the cloud shedding mechanism was driven by a shock wave, a low frequency associated with spanwise structures is observed.

Besides these experimental investigations, numerical simulations were performed to investigate such 3D unsteady cavitating flows on hydrofoils and venturis, based on mixture homogeneous models (one-fluid methods). Various assumptions were done on the viscous effects and the turbulence modelling. Inviscid compressible codes have been developped to simulate a 3D twisted hydrofoil (Schnerr *et al.* (2008); Koop & Hoeijmakers (2010)). Since few years, Large Eddy Simulations (LES) were tested on both hydrofoil and Venturi geometries (Wang & Ostoja-Starzewski (2007); Dittakavi *et al.* (2010)). To overcome the high computational cost of a wall resolved LES, a wall model based on the logarithmic wall law was introduced in an implicit LES solver (Bensow & Bark (June 2010)). In the same way, Kunz (Kinzel *et al.* (2007) performed Detached-Eddy Simulation (DES). Recently, the Partial-Averaged Navier-Stokes (PANS) approach based on a $k-\varepsilon$ turbulence model was tested for a cavitating flow around a marine propeller (Ji *et al.* (2012)).

The present work follows studies performed at the LEGI to develop an in-house finite-volume code solving the URANS compressible equations with a mixture homogeneous approach. The cavitation phenomenon was modeled by a barotropic liquid-vapor mixture equation of state (EOS) (Goncalves & Patella (2009); Goncalves (2011)). Recently, an hybrid RANS/LES approach able to adjust the level of turbulent eddy viscosity was developed and validated on 2D Venturi flows (Decaix & Goncalves (2011)). This approach was introduced in the Spalart-Allmaras model. This model is compared with the DES approach of Spalart by performing 3D computations of a venturi cavitating flow.

FLOW MODELLING

The homogeneous approach

The homogeneous mixture approach is used to model two-phase flows. In addition, the phases are assumed to be in thermal and mechanical equilibrium: they share the same temperature T and the same pressure P. By introducing α_k the averaged fraction of presence of phase k. The density ρ, the center of mass velocity u and the internal energy e for the mixture are defined by:

$$\rho = \sum_k \alpha_k \rho_k \tag{1}$$

$$\rho u_i = \sum_k \alpha_k \rho_k u_{k,i} \tag{2}$$

$$\rho e = \sum_k \alpha_k \rho_k e_k \tag{3}$$

The cavitation model

To link the pressure to the thermodynamic variables, the stiffened gas EOS is used for pure phases. In the mixture, a barotropic law is considered (Delannoy & Kueny (1990)). When the pressure is between $P_{vap} + \Delta P$ and $P_{vap} - \Delta P$, the following relationship applies:

$$P(\alpha) = P_{vap} + \left(\frac{\rho_L^{sat} - \rho_V^{sat}}{2}\right) c_{baro}^2 \operatorname{Arcsin}(1-2\alpha) \tag{4}$$

Reynolds-Averaged Navier-Stokes equations

For turbulent computations, the Reynolds-Averaged Navier-Stokes equations are used, coupled with one or two-equation turbulence models. For low Mach number applications, an inviscid preconditioning method is necessary (Guillard & Viozat (1999)), which implies the presence of the matrix P_c.

$$P_c^{-1}\frac{\partial w}{\partial t} + \operatorname{div}(F_c - F_v) = S \tag{5}$$

$$w = \begin{pmatrix} \rho \\ \rho V \\ \rho E \\ \rho k \\ \rho \Psi \end{pmatrix} \quad F_c = \begin{pmatrix} \rho V \\ \rho V \otimes V + p\bar{\bar{I}} \\ (\rho E + p)V \\ \rho k V \\ \rho \Psi V \end{pmatrix} \quad F_v = \begin{pmatrix} 0 \\ \overline{\overline{\tau^v}} + \overline{\overline{\tau^t}} \\ (\overline{\overline{\tau^v}} + \overline{\overline{\tau^t}}).V - Q^v - Q^t \\ (\mu + \mu_t/\sigma_k)\operatorname{grad} k \\ (\mu + \mu_t/\sigma_\Psi)\operatorname{grad}\Psi \end{pmatrix}$$

where w denotes the conservative variables, F_c and F_v the convective and viscous flux densities and S the source terms, which concern only the transport equations. k is the mixture turbulent kinetic energy and Ψ is a mixture turbulent variable.
The exact expression of the eddy-viscosity μ_t and the source terms depends on the turbulence model as well as constants σ_k and σ_Ψ.
The total stress tensor $\overline{\overline{\tau}}$ is evaluated using the Stokes hypothesis, Newton's law and the Boussinesq assumption. The total heat flux vector Q is obtained from the Fourier law involving a turbulent thermal conductivity λ_t with the constant Prandtl number hypothesis.

$$\overline{\overline{\tau}} = \overline{\overline{\tau^v}} + \overline{\overline{\tau^t}} = (\mu+\mu_t)\left[(\operatorname{grad} V + (\operatorname{grad} V)^t) - \frac{2}{3}(\operatorname{div} V)\bar{\bar{I}}\right] - \frac{2}{3}\rho k \bar{\bar{I}}$$

$$Q = Q^v + Q^t = -(\lambda+\lambda_t)\operatorname{grad} T \quad \text{with} \quad \lambda_t = \frac{\mu_t C_p}{P_{rt}} \tag{6}$$

In pure liquid, the viscosity μ is determined by an exponential law and, in pure vapour, the viscosity follows the Sutherland law.

$$\mu_L(T) = \mu_{0_L}\exp(B/T) \tag{7}$$

$$\mu_V(T) = \mu_{0_V}\sqrt{\frac{T}{293}}\frac{1+T_S/293}{1+T_S/T} \tag{8}$$

where μ_{0_L}, μ_{0_V}, B and T_S are constants.
The mixture viscosity and the mixture thermal conductivity λ are defined as the arithmetic mean of the liquid and vapour values:

$$\mu(T,\alpha) = \alpha\mu_V(T) + (1-\alpha)\mu_L(T) \tag{9}$$

$$\lambda(\alpha) = \alpha\frac{\mu_V C_{p_V}}{P_{r_V}} + (1-\alpha)\frac{\mu_L C_{p_L}}{P_{r_L}} \tag{10}$$

The turbulent Prandtl number P_{rt} is set to 1.

Turbulence modelling

In the present work, the DES model (Spalart *et al.* (1997)) is applied following formulation for the pseudo viscosity $\tilde{\nu}$:

$$\frac{\partial \rho\tilde{\nu}}{\partial t} + \frac{\partial}{\partial x_l}\left[\rho u_l \tilde{\nu} - \frac{1}{\sigma}(\mu+\rho\tilde{\nu})\frac{\partial\tilde{\nu}}{\partial x_l}\right] = c_{b1}(1-f_{t2})\tilde{S}\rho\tilde{\nu} + \frac{c_{b2}}{\sigma}\frac{\partial\rho\tilde{\nu}}{\partial x_l}\frac{\partial\tilde{\nu}}{\partial x_l} - \left(c_{\omega 1}f_\omega - \frac{c_{b1}}{\kappa^2}f_{t2}\right)\frac{\tilde{\nu}^2}{\tilde{d}^2} \tag{11}$$

with $\tilde{d} = \min(d, C_{DES}\Delta)$ the new distance to walls, where d is the distance from the nearest wall, $\Delta = \max(\Delta x, \Delta y, \Delta z)$ and $C_{DES} = 0.9$ for cavitating regions after some tests.
Inspiring from the Menter's works (Menter (2010)), the Spalart and Allamras model is transformed to behave as a SAS model. This is done by replacing the distance d by the von Karman lenght scale in the destruction term. The model reads:

$$\frac{\partial \rho\tilde{\nu}}{\partial t} + \frac{\partial}{\partial x_l}\left[\rho u_l \tilde{\nu} - \frac{1}{\sigma}(\mu+\rho\tilde{\nu})\frac{\partial\tilde{\nu}}{\partial x_l}\right] = c_{b1}(1-f_{t2})\tilde{S}\rho\tilde{\nu} + \frac{c_{b2}}{\sigma}\frac{\partial\overline{\rho}\tilde{\nu}}{\partial x_l}\frac{\partial\tilde{\nu}}{\partial x_l} - c_{\omega 1}f_\omega\overline{\rho}\,\xi_{sas}\frac{\tilde{\nu}^2}{L_{vk}^2} - \frac{c_{b1}}{\kappa^2}f_{t2}\rho\frac{\tilde{\nu}^2}{d^2} \tag{12}$$

with ξ_{SAS} a constant to specify. In the present work, the use of L_{vk} instead of d is applied only in two-phase flow regions and after several tests, the constant ξ_{SAS} is set to 3.

Wall functions

At the wall, a two-layer wall law is used:

$$u^+ = y^+ \quad \text{if } y^+ < 11.13$$

$$u^+ = \frac{1}{\kappa}\ln y^+ + 5.25 \quad \text{if } y^+ > 11.13$$

$$u^+ = \frac{u}{U_\tau}\ ;\ y^+ = \frac{yU_\tau}{\nu_w}\ ;\ U_\tau = \sqrt{\frac{\tau_w}{\rho_w}}$$

where $\kappa = 0.41$ is the von Karman constant and the subscript w indicates wall values. We assume that wall functions are similar in a two-phase flow and in a single-phase flow.

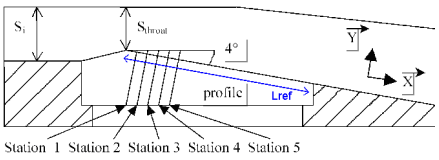

Figure 1. Schematic view of the Venturi.

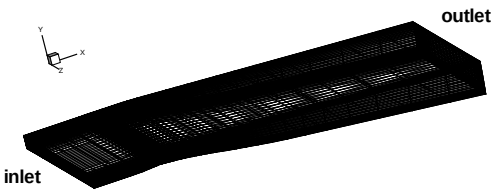

Figure 2. View of the 3D mesh.

NUMERICAL METHOD

The numerical simulations are carried out using an implicit CFD code solving the RANS/turbulent systems for multi-domain structured meshes. This solver is based on a cell-centered finite-volume discretization. For the mean flow, the convective flux density vector on a cell face is computed with the Jameson-Schmidt-Turkel scheme in which the dispersive error is cancelled. It allows to reach the third-order space accuracy. The viscous terms are discretized by a second-order space-centered scheme. For the turbulence transport equations, the upwind Roe scheme is used to obtain a more robust method. The second-order accuracy is obtained by introducing a flux-limited dissipation.
Time integration is achieved using the dual time stepping approach and a low-cost implicit method consisting in solving, at each time step, a system of equations arising from the linearization of a fully implicit scheme. The derivative with respect to the physical time is discretized by a second-order formula (more details in Goncalves & Patella (2009).).

FLOW AND COMPUTATION CONFIGURATIONS

Experimental conditions

The test case is a Venturi geometry (Fig.1) characterized by a divergence angle of 4°. The edge forming the throat of the Venturi is used to fix the separation point of the cavity. Five stations of measurement are settled along the bottom wall.

The selected operating point is characterized by the following physical parameters (Barre *et al.* (2009)):

- U_{inlet} = 10.8 m/s, the inlet velocity
- $\sigma_{inlet} = \dfrac{P_{inlet} - P_{vap}}{0.5\rho U_{inlet}^2} \simeq 0.55$, the cavitation parameter in the inlet section
- $T_{ref} \simeq 293K$, the reference temperature
- L_{ref}=252 mm, the reference length, which corresponds to the chord of a blade of a turbomachinery
- $Re_{L_{ref}} = \dfrac{U_{inlet} L_{ref}}{\nu} = 2.7\,10^6$, the Reynolds number

With these parameters, a cavity length L ranging from 70 mm to 85 mm is obtained. The cavity is characterized by an almost constant length, although the closure region always fluctuates, with the presence of a re-entrant jet and little vapour cloud sheddings. For this geometry, no periodic cycles with large sheddings were observed.
The exprimental measurements were made in the mid span and give:

- the mean longitudinal velocity and mean void fraction at the 5 stations
- the mean pressure and rms pressure fluctuations along the bottom wall

Mesh and numerical set up

A 3D mesh was built from the 2D meshes investigated previously (Goncalves & Decaix (2012)). The 3D mesh contains: 251 nodes in the flow direction and 62 nodes in each transversal direction (Fig.2). The y^+ values obtained from a non cavitating computation with the SA turbulence model vary between 1 and 20. The computation is performed with a two step method. First a cavitating flow is computed with a local time step. Then, when the flow reach a developed state, the unsteady cavitating regime is computed with the dual time stepping method. The numerical parameters are:

- the dimensionless time step, $\Delta t^* = \dfrac{\Delta t U_{inlet}}{L_{ref}} = 4.9\,10^{-3}$
- number of sub-iterations for the dual time stepping method, 100
- the CFL number, 0.2
- Jacobi iterations for the implicit stage, 15
- the two coefficients of the artificial dissipation, $k^{(2)} = 1$ and $k^{(4)} = 0.055$
- the farfield value of the turbulent kinetic energy, $k_\infty = 0.0045$ m^2/s^2
- the farfield value of the turbulent eddy-viscosity, $\mu_{t_\infty} = 10^{-4}$ Pa.s

RESULTS

Two computations were performed: one with the DES model and another with the SAS model. Both computations have the same inlet cavitation parameter $\sigma_{inlet} = 0.6$ close to the experimental one.

Comparison between the experiment and computations

The 3D computations can be compared with experimental measurements only in the mid-span sec-

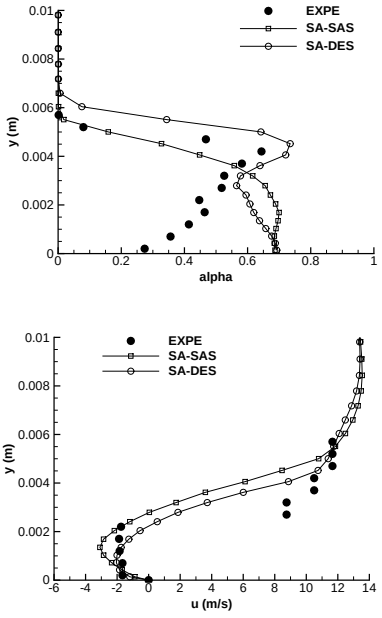

Figure 3. Time-averaged void fraction (top) and longitudinal velocity (bottom) at station 3.

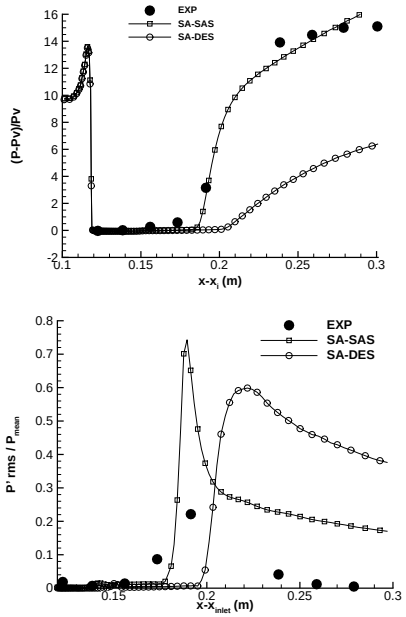

Figure 4. Time-average wall pressure (top) and RMS wall pressure fluctuations (bottom).

tion since no measurements are available elsewhere. At the first two stations, an attached cavitation sheet is observed, whereas at the third last stations, a re-entrant jet is present leading to an unsteady cavity with cloud sheddings. Most of the standard turbulence models are not able to capture the re-entrant and often predict a steady cavitation sheet. In the present works, the two computations predict a cavitation sheet in agreement with the experimental observations with:

- an attached cavity at stations 1 and 2 (not shown here),
- a re-entrant jet from station 3 to 5 (Fig.3)

The mean pressure and the rms pressure fluctuations along the bottom wall make appear large discrepancies between the experiment and the computations and also between the computations (Fig.4). The SAS computation is close to the experimental mean pressure profile, which is not the case for the DES computations due to the convection of small vapour clouds downstream. The RMS pressure fluctuations differ largely between the experiment and the computations. The amplitude of the fluctuation peak is overstimated by a factor greater than 2.5 compared to the experiment. Downstream the cavity, a high level of pressure fluctuations is maintained, which is not observed experimentally. An explication for these discrepancies may come from the 3D dynamic behaviour of the cavities computed as described below.

Global features of the 3D cavitation sheet

A Direct Fourier Transform (DFT) of the vapour volume put in evidence a low frequency around 6 Hz. Such a frequency is not observed experimentally. Therefore, the recent results provided by Prothin (Prothin *et al.* (2012)) show a bifurcation of the shedding mechanism around the value $\frac{\sigma}{2\beta} \approx 4$ (with β the angle of attack). For a lower value, the shedding mecanism would be driven by a shock wave, which propagates along the cavitation sheet closure. In this case, a low frequency associated with spanwise structures is observed. For our Venturi test case, the value $\frac{\sigma}{2\beta}$ ($\beta = 4°$) is closed to 4, near the regime transition. Therefore a low frequency phenomenon can be expected.

A global analysis of the flow downstream the cavitation sheet makes appear a periodic unsteady mode of the cross velocity w (Fig.5). Again, a DFT of the cross velocity signal shows the presence of the low frequency around 6 Hz. Nevertheless, the SAS and DES computations differ one from each other by the behaviour of the cavitation sheet. In the case of the DES computation, the cavity is more stable with a U-shape form of the cavity (Fig.6), whereas the SAS computations leads to a cross instability of the cavity (Fig.7) To explain the SAS behaviour, an analysis of the flow inside the cavity has been performed. First, spatial correlations based on the void fraction and the longitudinal velocity between two point located on each side of the venturi (Fig.8) show that the two signals superimposed. Consequently, the cavitation sheet behaviour is correlated to the velocity field evolution and particularly to the re-entrant jet. Furthermore, the two signals show again the low frequency. By plotting the void fraction and the velocity field at three different instants in a cross plane located at the station 3 (Fig.9), further flow characteristics can be displayed. Closed to the side wall, a vortex is observed, whereas the flow inside the cav-

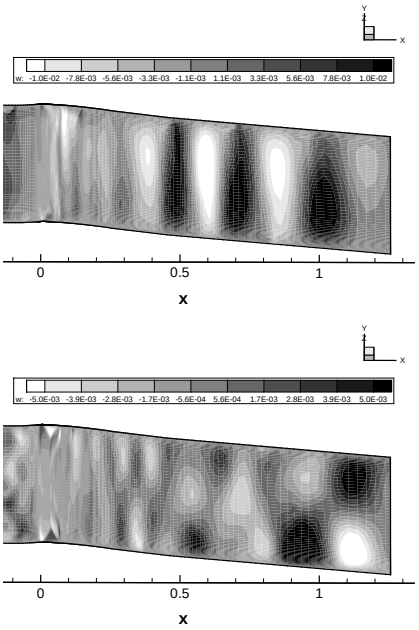

Figure 5. Cross component w of velocity field, SA-SAS (top) and SA-DES (bottom).

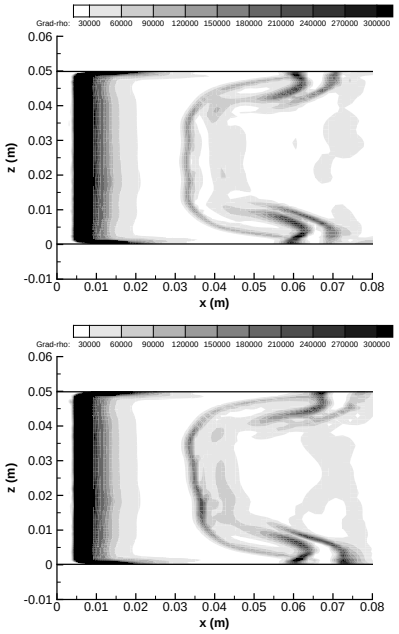

Figure 6. Gradient density modulus visualization at two different instants: DES computation.

ity shows a cross component w that changes direction with time. It is noticeable that outside the cavity no cross flow is observed. From these features, a mechanism for the unstable behaviour of the cavitation sheet can be drawn. Due to the presence of the side wall, two vortices on each side are formed. These vortices increase the momentum quantity of the flow closed to the wall compared to the mid-span section. Therefore two consequences are involved:

- the flow along the side wall is less sensitive to the re-entrant jet, which is deviated to the centre

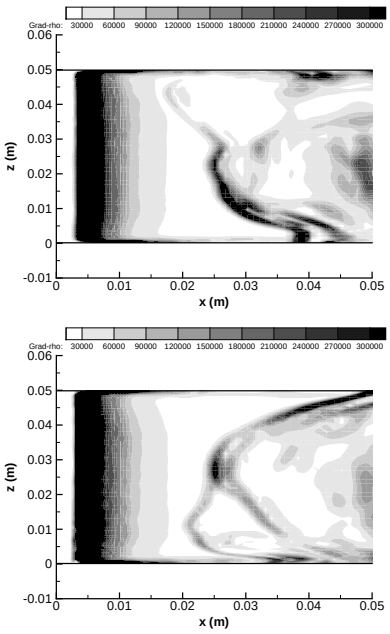

Figure 7. Gradient density modulus visualization at two different instants: SAS computation.

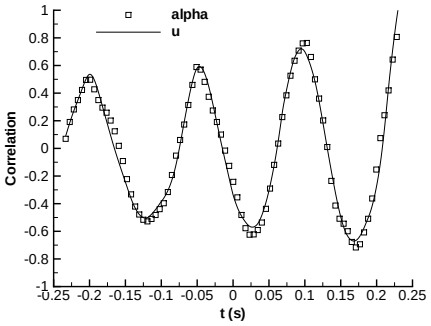

Figure 8. Spatial correlations based on the void fraction and the longitudinal velocity between two points located on each side of the Venturi (SAS computation).

- the low pressure in the vortex core tends to increase the void fraction along the side wall.

These two features explain the U-shape form of the cavitation sheet (DES computation).
The unstable behaviour of the cavitation sheet (SAS computation) provides from an alternate destablization of the vortices due to the re-entrant and side entrant jets.

CONCLUSION

A 3D cavitation sheet has been computed applying an homogeneous approach for the two-phase mixture coupled with an hybrid RANS/LES turbulence modelling (DES ans SAS models). The results compared with the experiment show a good agreement in the case of the time-averaged longitudinal velocity and void fraction. On the contrary, the pressure data show discrepancies that are related with a differ-

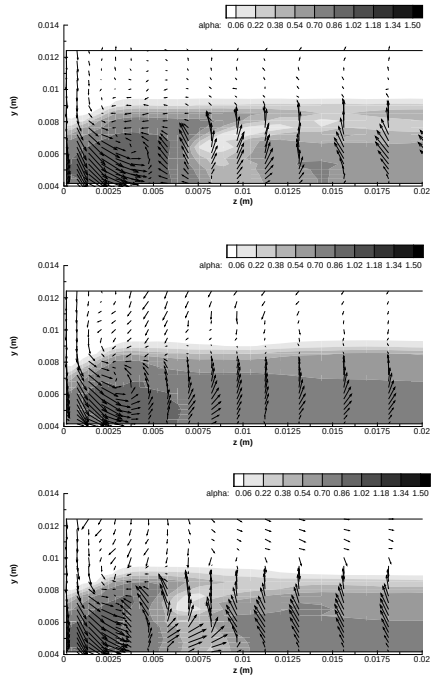

Figure 9. Snapshots of the void ratio and the velocity vector in a transversal cutting plane at station 3 (SAS computation).

ent dynamic behaviour of the cavity.

The computation predict a low frequency, which can be link to the recent results of Prothin (Prothin *et al.* (2012)). In the present configuration, a mechanism to explain this low frequency is proposed by involving the role plays by the vortices along the side walls. The vortices perturb the re-entrant jet and an asymmetric destabilization of the re-entrant jet drives to the oblique mode described.

REFERENCES

Barre, S., Rolland, J., Boitel, G., Goncalves, E. & Patella, R. Fortes 2009 Experiments and modelling of cavitating flows in Venturi: attached sheet cavitation. *European Journal of Mechanics B/Fluids* **28**, 444–464.

Bensow, R. & Bark, G. June 2010 Simulating cavitating flows with LES in openfoam. In *V ECCOMAS CFD, Lisbon, Portugal*.

Decaix, J. & Goncalves, E. 2011 Time-dependent simulation of cavitating flow with $k-\ell$ turbulence models. *Int. Journal for Numerical Methods in Fluids* Online, DOI:10.1002/fld.2601.

Delannoy, Y. & Kueny, JL. 1990 Two phase flow approach in unsteady cavitation modelling. In *Cavitation and Multiphase Flow Forum, ASME-FED, vol. 98, pp.153-158*.

Dittakavi, N., Chunekar, A. & Frankel, S. 2010 Large eddy simulation of turbulent-cavitation interactions in a Venturi nozzle. *Journal of Fluids Engineering* **132** (12), 121301.

Foeth, E.J., van Doorne, C.W, van Terwisga, T. & Wienecke, B. 2006 Time-resolved PIV and flow visualization of 3D sheet cavitation. *Experiments in Fluids* **40**, 503–513.

Goncalves, E. 2011 Numerical study of unsteady turbulent cavitating flows. *European Journal of Mechanics B/Fluids* **30** (1), 26–40.

Goncalves, E. & Decaix, J. 2012 Wall model and mesh influence study for partial cavities. *European Journal of Mechanics B/Fluids* **31** (1), 12–29.

Goncalves, E. & Patella, R. Fortes 2009 Numerical simulation of cavitating flows with homogeneous models. *Computers & Fluids* **38** (9), 1682–1696.

Guillard, H. & Viozat, C. 1999 On the behaviour of upwind schemes in the low Mach number limit. *Computers & Fluids* **28** (1), 63–86.

Ji, B., Luo, X., Peng, X. & Xu, H. 2012 Partially-averaged Navier-Stokes method with modified $k-\varepsilon$ model for cavitating flow around a marine propeller in a non-uniform wake. *Int. Journal of Heat and Mass Transfer* **55**, 6582–6588.

Kinzel, M., Lindau, J., Peltier, L., Kunz, R. & Venkateswaran, S. 2007 Detached-eddy simulations for cavitating flows. In *AIAA-2007-4098, 18^{t}h AIAA Computational Fluid dynamics Conference, Miami, USA*.

Koop, A.H. & Hoeijmakers, H.W. 2010 Unsteady sheet cavitation on three-dimensional hydrofoil. In *7th International Conference on Multiphase Flow, Tampa, USA*.

Laberteaux, K.R. & Ceccio, S.L. 2001 Partial cavity flows. Part1. Cavities forming on models without spanwise variation. *Journal of Fluid Mechanics* **431**, 1–41.

de Lange, D.F. & de Bruin, G.J. 1998 Sheet cavitation and cloud cavitation, re-entrant jet and three-dimensionality. *Applied Scientific Research* pp. 91–114.

Menter, F.R. 2010 The scale-adaptive simulation method for unsteady turbulent flow predictions. Part 1: Theory and model description. *Flow, Turbulence and Combustion* **85** (1), 113–138.

Prothin, S., Billard, J-Y. & Djeridi, H. 2012 Image processing using POD and DMD for the study of cavitation development on a NACA0015. In *13th Journées de l'Hydrodynamique, Laboratoire Saint-Venant, Chatou, France*.

Schnerr, G.H., Sezal, I.H. & Schmidt, S.J. 2008 Numerical investigation of three-dimensional cloud cavitation with special emphasis on collapse induced shock dynamics. *Physics of Fluids* **20**, 040703.

Spalart, P.R., Jou, W.H, Strelets, M. & Allmaras, S.R. 1997 Comments on the feasibility of LES for wings and on hybrid RANS//LES approach. In *1st AFSOR Int. Conf. on DNS/LES - Ruston*.

Wang, G. & Ostoja-Starzewski, M. 2007 Large eddy simulation of a sheet/cloud cavitation on a NACA0015 hydrofoil. *Applied Mathematical Modeling* **31**, 417–447.